Li *et al. Satellite Navigation* (2022) 3:7
https://doi.org/10.1186/s43020-022-00068-0

Satellite Navigation
https://satellite-navigation.springeropen.com/

ORIGINAL ARTICLE Open Access

Principle and performance of multi-frequency and multi-GNSS PPP-RTK

Xingxing Li[1], Bo Wang[1], Xin Li[1*], Jiaxin Huang[2], Hongbo Lyu[1] and Xinjuan Han[1]

Abstract

PPP-RTK which takes full advantages of both Real-Time Kinematic (RTK) and Precise Point Positioning (PPP), is able to provide centimeter-level positioning accuracy with rapid integer Ambiguity Resolution (AR). In recent years, with the development of BeiDou Navigation Satellite System (BDS) and Galileo navigation satellite system (Galileo) as well as the modernization of Global Positioning System (GPS) and GLObal NAvigation Satellite System (GLONASS), more than 140 Global Navigation Satellite System (GNSS) satellites are available. Particularly, the new-generation GNSS satellites are capable of transmitting signals on three or more frequencies. Multi-GNSS and multi-frequency observations become available and can be used to enhance the performance of PPP-RTK. In this contribution, we develop a multi-GNSS and multi-frequency PPP-RTK model, which uses all the available GNSS observations, and comprehensively evaluate its performance in urban environments from the perspectives of positioning accuracy, convergence and fixing percentage. In this method, the precise atmospheric corrections are derived from the multi-frequency and multi-GNSS observations of a regional network, and then disseminated to users to achieve PPP rapid AR. Furthermore, a cascade ambiguity fixing strategy using Extra-Wide-Lane (EWL), Wide-Lane (WL) and L1 ambiguities is employed to improve the performance of ambiguity fixing in the urban environments. Vehicle experiments in different scenarios such as suburbs, overpasses, and tunnels are conducted to validate the proposed method. In suburbs, an accuracy of within 2 cm in the horizontal direction and 4 cm in the vertical direction, with the fixing percentage of 93.7% can be achieved. Compared to the GPS-only solution, the positioning accuracy is improved by 87.6%. In urban environments where signals are interrupted frequently, a fast ambiguity re-fixing can be achieved within 5 s. Moreover, multi-frequency GNSS signals can further improve the positioning performance of PPP-RTK, particularly in the case of small amount of observations. These results demonstrate that the multi-frequency and multi-GNSS PPP-RTK is a promising tool for supporting precise vehicle navigation.

Keywords: Multi-frequency, Multi-GNSS, PPP-RTK, Rapid ambiguity resolution, Vehicle navigation

Introduction

With the development of emerging technologies such as autonomous driving, mass-market applications are in urgent need of fast, high-precision, and low-bandwidth location services (European GNSS Agency, 2019). Precise Point Positioning (PPP), as one of the mainstream Global Navigation Satellite System (GNSS) positioning technologies, is able to achieve centimeter-level positioning accuracy globally using a single receiver (Zumberge et al., 1997; Kouba and Héroux 2001). However, it needs several minutes to initialize, which inhibits its application in the mass-market (Geng et al., 2020; Li et al., 2018, 2019). Recently, a PPP-RTK method that exploits the precise atmospheric corrections from a regional network to enable rapid Ambiguity Resolution (AR) was proposed (Li et al., 2013; Teunissen et al., 2010; Wubbena et al., 2005). The PPP-RTK technique exhibits unique advantages in terms of convergence, accuracy, and real-time communication,

*Correspondence: xinli@sgg.whu.edu.cn
[1] School of Geodesy and Geomatics, Wuhan University, 129 Luoyu Road, Wuhan 430079, China
Full list of author information is available at the end of the article

which has become a forefront subject in the field of vehicle navigation.

The concept of PPP-RTK was firstly proposed by Wubbena et al. (2005), aiming to achieve centimeter-level positioning accuracy in a few seconds in post-processing and real-time applications with the augmentations from regional networks. Later, Teunissen et al. (2010), Li et al. (2011), and Zhang et al. (2011) established the prototypes of the PPP-RTK system respectively, which commonly have two parts: on the server side, the precise orbit, clock, phase bias as well as the atmospheric corrections are generated based on the observations of a regional network; on the user side, fast AR of absolute positioning is realized with the corrections from the network. The atmospheric modeling and bias correcting in PPP-RTK were first studied by academia (Li et al, 2014; Oliveira et al., 2017; Zhang et al, 2019)., and then PPP-RTK method has come into practical applications. The Japanese Quasi-Zenith Satellite System (QZSS) is the first system to implement a satellite-based PPP-RTK augmentation service—Centimeter Level Augmentation Service (CLAS) (Cabinet Office, 2020). In addition, some commercial companies have also provided PPP-RTK services, e.g., Trimble CenterPoint RTX-FAST, NovAtel TerraStar-X, Ublox PointPerfect, etc.. However, most of the services adopt dual-frequency observations, and their performances in real-time kinematic positioning need improving.

In recent years, with the development of BeiDou Navigation Satellite System (BDS) and Galileo navigation satellite system (Galileo) as well as the modernization of Global Positioning System (GPS) and GLObal NAvigation Satellite System (GLONASS) (Li et al., 2019; Montenbruck et al., 2014; Ren et al., 2021), more than 140 GNSS satellites are available and new-generation GNSS satellites are capable of transmitting signals on three or more frequencies. It has been demonstrated that the convergence, accuracy and reliability of PPP AR can be significantly improved by multi-GNSS fusion (Jokinen et al., 2013; Liu et al., 2017). The Time to First Fix (TTFF) can be shortened to 10 min when the observations of GPS/GLONASS/Galileo/BDS were adopted (Li et al., 2018). At the same time, the studies show that the performance of PPP AR can be effectively improved when multi-frequency observations are adopted (Geng & Bock, 2013; Gu et al., 2015; Li et al., 2018). Li et al. (2019) found that the triple-frequency Galileo/BDS-2 (BeiDou-2 Navigation Satellite System) PPP AR can converge to centimeter-level positioning accuracy in about 10 min. Multi-frequency and multi-GNSS observations bring more possibilities for enhancing the performance of PPP-RTK.

In this contribution, we developed a multi-frequency and multi-GNSS PPP-RTK model, which uses all the available GNSS observations, to achieve rapid positioning with the accuracy at centimeter-level for vehicle navigation in urban environments. In addition, several vehicle experiments were conducted in different scenarios such as suburbs, overpasses, and tunnels to comprehensively verify the effectiveness of the proposed model. The benefits of multi-frequency and multi-GNSS observations used for PPP-RTK are analyzed in terms of the accuracy, convergence, and fixing percentage. This study is organized as follows: Sect. 2 introduces the algorithm of the multi-frequency and multi-GNSS PPP-RTK system in detail. Section 3 provides the experimental procedures and the data processing strategies in the vehicle experiments. Section 4 evaluates the performance of the multi-frequency and multi-GNSS PPP-RTK and analyzes its results in different scenarios. Section 5 gives conclusions and outlooks.

Method

Multi-frequency and multi-GNSS PPP-RTK system

The procedure of the multi-frequency and multi-GNSS PPP-RTK system is illustrated in Fig. 1. On the server side, given precise satellite orbits and clocks, PPP is conducted at all stations of the regional network. Then, the satellite phase biases, also known as the Uncalibrated Phase Delays (UPDs), of Extra-Wide-Lane (EWL), Wide-Lane (WL), and Narrow-Lane (NL) are estimated by the method proposed by Li, Han, et al. (2021). Therewith, the multi-frequency and multi-GNSS PPP AR is carried out to extract the precise atmospheric corrections. On the user side, the atmospheric corrections of the user side are interpolated using the atmospheric corrections from the server side. When the satellite orbits and clocks, UPDs,

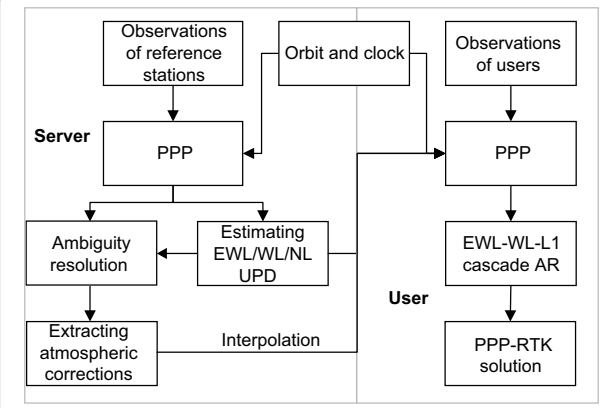

Fig. 1 Flow chart of multi-frequency and multi-GNSS PPP-RTK system

and the external atmospheric corrections are received, PPP and EWL-WL-L1 cascade AR are implemented, and finally the multi-frequency and multi-GNSS PPP-RTK is achieved. In the following sections, the algorithms for atmospheric correction extraction based on the uncombined PPP model on the server side, and for EWL-WL-L1 cascade AR with external atmospheric corrections on the user side are described.

Atmospheric correction extraction based on uncombined PPP AR model

The GNSS pseudorange observation ($P^s_{r,n}$) and phase observation($L^s_{r,n}$) are described as:

$$\begin{aligned} P^s_{r,k} =& \rho^s_r + c(t_r - t^s) + \gamma_k \cdot I^s_{r,1} + m^s_r \cdot \\ & Z_r + (b_{r,k} - b^s_k) + e^s_{r,k} \\ L^s_{r,k} =& \rho^s_r + c(t_r - t^s) - \gamma_k \cdot I^s_{r,1} + m^s_r \cdot \\ & Z_r + \lambda_k(B_{r,k} - B^s_k) + \lambda_k \cdot N^s_{r,k} + \varepsilon^s_{r,k} \end{aligned} \tag{1}$$

where the superscripts s, r and k represent satellite, receiver, and frequency, respectively; ρ^s_r is the geometric distance between the phase centers of the satellite antenna and the receiving antenna; c is the vacuum speed of light; t_r and t^s denote the receiver and satellite clock offset, respectively; $I^s_{r,1}$ refers to the ionospheric propagation delay of a GNSS signal on the first frequency; γ_k is the frequency-dependent multiplier factor, which can be expressed as $\gamma_k = \lambda_k/\lambda_1$; $m^s_r \cdot Z_r$ represents tropospheric path delay; $b_{r,k}$ and b^s_k are the code hardware delays while $B_{r,k}$ and B^s_k are the phase delays of receiver and satellite, respectively; $N^s_{r,k}$ represents the integer ambiguity; $e^s_{r,k}$ and $\varepsilon^s_{r,k}$ are the sum of measurement noise and multipath error of code and phase observations, respectively. It should be noted that other errors such as relativistic effects, Sagnac effect, solid earth tide, polar tides, ocean tide loadings, satellite and receiver antenna Phase Center Offsets (PCOs) and Phase Center Variations (PCVs), and phase wind-up are corrected by the known models (Kouba, 2015).

The uncombined PPP model is implemented to derive the precise tropospheric and ionospheric delays directly when ambiguity is fixed (Zhang et al. 2012). The general equations of the multi-frequency undifferenced PPP model can be written as:

$$\begin{cases} p^s_{r,i} = \mu^s_r \cdot x + \hat{t}_r - \overline{t}^s_{\mathrm{IF}} + \gamma_i \cdot \hat{I}^s_{r,i} + m^s_{r,w} Z_{r,w} + e^s_{r,k} \\ p^s_{r,j} = \mu^s_r \cdot x + \hat{t}_r - \overline{t}^s_{\mathrm{IF}} + \gamma_j \cdot \hat{I}^s_{r,i} + m^s_{r,w} Z_{r,w} + e^s_{r,k} \\ p^s_{r,k} = \mu^s_r \cdot x + \hat{t}_r - \overline{t}^s_{\mathrm{IF}} + \gamma_k \cdot \hat{I}^s_{r,i} + m^s_{r,w} Z_{r,w} + B^{\mathrm{IFB}}_k + e^s_{r,k} \end{cases} \tag{2}$$

$$\begin{cases} l^s_{r,i} = \mu^s_r \cdot x + \hat{t}_r - \overline{t}^s_{\mathrm{IF}} - \gamma_i \cdot \hat{I}^s_{r,i} + m^s_{r,w} Z_{r,w} + \lambda_i \hat{N}^s_{r,i} + \varepsilon^s_{r,i} \\ l^s_{r,j} = \mu^s_r \cdot x + \hat{t}_r - \overline{t}^s_{\mathrm{IF}} - \gamma_j \cdot \hat{I}^s_{r,i} + m^s_{r,w} Z_{r,w} + \lambda_j \hat{N}^s_{r,j} + \varepsilon^s_{r,j} \\ l^s_{r,k} = \mu^s_r \cdot x + \hat{t}_r - \overline{t}^s_{\mathrm{IF}} - \gamma_k \cdot \hat{I}^s_{r,i} + m^s_{r,w} Z_{r,w} + \lambda_k \hat{N}^s_{r,k} + \varepsilon^s_{r,k} \end{cases} \tag{3}$$

With

$$\begin{cases} k \neq i, k \neq j, \alpha_{ij} = \dfrac{f_i^2}{f_i^2 - f_j^2}, \beta_{ij} = \dfrac{f_j^2}{f_i^2 - f_j^2} \\ \overline{t}^s_{\mathrm{IF}} = c \cdot t^s + \left(\alpha_{ij} b^s_i + \beta_{ij} b^s_j\right) \\ \hat{t}_r = c \cdot t_r + \left(\alpha_{ij} b_{r,i} + \beta_{ij} b_{r,j}\right) \\ \hat{I}^s_{r,i} = I^s_{r,i} + \beta_{ij}\left(b_{r,i} - b_{r,j}\right) - \beta_{ij}\left(b^s_i - b^s_j\right) \\ B^{\mathrm{IFB}}_k = \left[\left(b_{r,k} - b^s_k\right) - \left(b_{r,i} - b^s_i\right)\right] + \dfrac{\beta_{ij}}{\beta_{ik}}\left[\left(b_{r,i} - b^s_i\right) - \left(b_{r,j} - b^s_j\right)\right] \\ \hat{N}^s_{r,i} = N^s_{r,i} + \left(B_{r,i} - B^s_i\right) + \left[b^s_{\mathrm{IF}} - b_{r,\mathrm{IF}} + \beta_{ij}\left(b_{r,i} - b_{r,j}\right) - \beta_{ij}\left(b^s_i - b^s_j\right)\right]/\lambda_i \\ \hat{N}^s_{r,j} = N^s_{r,j} + \left(B_{r,j} - B^s_j\right) + \left[b^s_{\mathrm{IF}} - b_{r,\mathrm{IF}} + \gamma_j\beta_{ij}\left(b_{r,i} - b_{r,j}\right) - \gamma_j\beta_{ij}\left(b^s_i - b^s_j\right)\right]/\lambda_j \\ \hat{N}^s_{r,k} = N^s_{r,k} + \left(B_{r,k} - B^s_k\right) + \left[b^s_{\mathrm{IF}} - b_{r,\mathrm{IF}} + \gamma_k\beta_{ij}\left(b_{r,i} - b_{r,j}\right) - \gamma_k\beta_{ij}\left(b^s_i - b^s_j\right)\right]/\lambda_k \end{cases} \tag{4}$$

where $p^s_{r,j}$ and $l^s_{r,j}$ represent the observed-minus-computed values of pseudorange and phase observations, respectively; μ^s_r is the unit vector from the receiver to the satellite; $\mathbf{x}$ ($\mathbf{x} = [\mathrm{d}x, \mathrm{d}y, \mathrm{d}z]$) denotes the receiver position increments vector relative to a prior position. B^{IFB}_k is the Inter-Frequency Bias (IFB), which describes the between-frequencies differences of code hardware delays. The code IFB at the frequency which is used for satellite clock estimation can be absorbed into the ionospheric delay, while the others are absorbed by setting an individual receiver clock parameter for each one. And the phase IFB can be absorbed into ambiguity (Montenbruck, et al. 2010; Pan, Zhang, et al., 2017; Pan et al., 2019). Another

bias that needs to be considered is the Inter-Frequency Clock Bias (IFCB), which is induced due to the inconsistency of the observations used for satellite clock estimation and precise positioning. The Code-specific IFCB (CIFCB) is usually eliminated by Differential Code Bias (DCB) transformation (Guo et al., 2015), while the Phase IFCB (PIFCB) is corrected by the corresponding corrections (Pan, Li, et al., 2017; Pan, Zhang, et al., 2017). For multi-GNSS PPP, a similar strategy with IFB is applied to compensate the Inter-System Bias (ISB) which represents the between-constellations differences of code hardware delays (Khodabandeh et al. 2016). After the precise satellite orbits, clocks, and UPDs are received, PPP AR is conducted in the reference network. Then the precise tropospheric delays and ionospheric delays are derived from the PPP AR solution directly, and broadcasted to users as atmospheric corrections.

$$\begin{cases} p^s_{r,n} = \mu^s_r \cdot x + \hat{t}_r - \overline{t}^s_{IF} + \gamma_n \cdot \hat{I}^s_{r,i} + m^s_{r,w} Z_{r,w} + \kappa \cdot B^{\mathrm{IFB}}_k + e^s_{r,n} \\ l^s_{r,n} = \mu^s_r \cdot x + \hat{t}_r - \overline{t}^s_{IF} - \gamma_n \cdot \hat{I}^s_{r,i} + m^s_{r,w} Z_{r,w} + \lambda_n \hat{N}^s_{r,n} + \varepsilon^s_{r,n} \\ l^s_I = \hat{I}^s_{r,n} - \tilde{I}^s_{r,n} = w_I, \quad w_I \sim \mathrm{N}(0, \sigma_I^2) \\ l^s_Z = Z_{r,w} - \tilde{Z}_{r,w} = w_Z, \quad w_Z \sim \mathrm{N}(0, \sigma_Z^2) \end{cases} \tag{5}$$

EWL-WL-L1 cascade AR with external atmospheric corrections

With the precise atmospheric corrections from a regional network, the Modified Linear Combination Method (MLCM) proposed by Li et al. (2011) is employed to interpolate the precise atmospheric corrections at the user side. As shown in Fig. 2, the external ionospheric and tropospheric corrections are introduced into the multi-frequency and multi-GNSS undifferenced PPP as virtual observation equations. Therefore, the PPP model with external atmospheric corrections is expressed as:

with the stochastic model

$$\Sigma = \mathrm{diag}(\sigma_p^2, \sigma_l^2, \sigma_I^2, \sigma_Z^2) \tag{6}$$

where κ is equal to 0 or 1, $\tilde{I}^s_{r,n}$ and $\tilde{Z}_{r,w}$ denote the precise ionospheric and tropospheric corrections, respectively; w_I and w_Z mean the differences between atmospheric corrections and actual atmospheric delays, which are the white noise with zero-mean and variance of σ_I^2 and σ_Z^2. After getting the PPP solution, the ambiguity at each frequency is acquired and then transformed to EWL and WL ambiguity according to Eq. (7).

$$\begin{bmatrix} \hat{N}^s_{\mathrm{EWL}\_jk} \\ \hat{N}^s_{\mathrm{WL}\_ij} \end{bmatrix} = \begin{bmatrix} 0 & 1 & -1 \\ 1 & -1 & 0 \end{bmatrix} \begin{bmatrix} \hat{N}^s_{r,i} \\ \hat{N}^s_{r,j} \\ \hat{N}^s_{r,k} \end{bmatrix} + \begin{bmatrix} d_{r,\mathrm{EWL}} - d^s_{\mathrm{EWL}} \\ d_{r,\mathrm{WL}} - d^s_{\mathrm{WL}} \end{bmatrix} \tag{7}$$

where d_r and d^s are the UPDs of receiver and satellite, respectively.

With the EWL, WL and NL UPDs products, the EWL, WL and L1 ambiguities are fixed sequentially. The phase biases of satellites are compensated with the corresponding UPD products, and those of receivers are eliminated through between-satellites differencing. Once the integer property is recovered, the ambiguity can be fixed by the LAMBDA search method (Teunissen 2010), and introduced to the PPP model as a virtual observation equation with an infinite weighting factor. The PPP model with the external EWL AR constraint is written as:

$$\begin{cases} p^s_{r,n} = \mu^s_r \cdot x + \hat{t}_r - \overline{t}^s_{\mathrm{IF}} + \gamma_{ik} \hat{I}^s_{r,i} + m^s_{r,w} Z_{r,w} + \kappa \cdot B^{\mathrm{IFB}}_k + e^s_{r,n} \\ l^s_{r,n} = \mu^s_r \cdot x + \hat{t}_r - \overline{t}^s_{\mathrm{IF}} - \gamma_{ik} \cdot \hat{I}^s_{r,i} + m^s_{r,w} Z_{r,w} + \hat{N}^s_{r,n} + \varepsilon^s_{r,n} \\ m = \Delta \hat{N}^{s_1 s_2}_{r,\mathrm{EWL}\_jk} = N^{s_1 s_2}_{r,\mathrm{EWL}\_jk} + d^{s_1 s_2}_{\mathrm{EWL}\_jk} \end{cases} \tag{8}$$

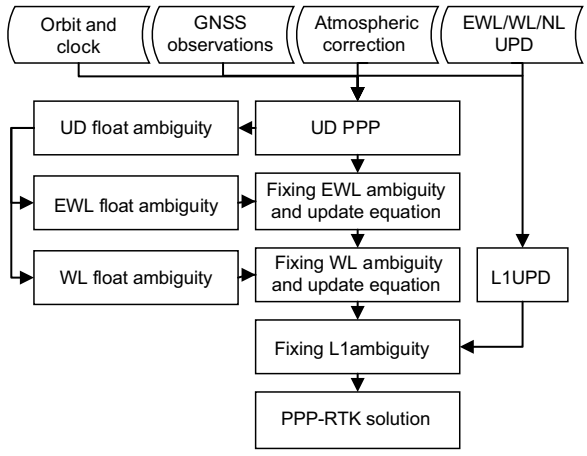

Fig. 2 Flow chart of EWL-WL-L1 cascade AR with external atmospheric corrections

with stochastic model

$$\Sigma = \mathrm{diag}\left(\sigma_p^2, \sigma_l^2, \sigma_m^2\right) \tag{9}$$

σ_m^2 is the variance of the virtual observation equation. The constraint decorrelates ambiguity and other parameters, which can accelerate convergence and provide accurate ambiguity. Similar to EWL AR, the WL ambiguity is fixed and involved in the PPP model as a virtual observation equation which can be expressed as:

$$l = \Delta\hat{N}_{r,\mathrm{WL}\_ij}^{s_1 s_2} = N_{r,\mathrm{WL}\_ij}^{s_1 s_2} + d_{r,\mathrm{WL}\_ij}^{s_1 s_2},\ \sigma_l^2 \in 0 \tag{10}$$

With those constraints, the accuracy of the PPP solution is improved and the search space of L1 ambiguity is narrowed. After L1 UPD is obtained by UPD transformation, L1 ambiguity is fixed. Finally, the multi-frequency and multi-GNSS PPP-RTK solution is derived.

Experiments

A vehicle experiment was conducted from 1:32 to 5:14 GPS Time (GPST) on March 18, 2021 to evaluate the performance of the proposed multi-frequency and multi-GNSS PPP-RTK method. As shown in Fig. 3a, 29 GNSS stations plotted by blue and red triangles in northern China were used to estimate UPDs. 10 GNSS stations (denoted by blue triangles in Fig. 3a) with an average spacing of about 30 km were selected to provide precise atmospheric corrections. Figure 3b shows the trajectories of the experimental vehicle. The first experiment was conducted in a suburban with an open-sky view, while the second one was in an urban area where the signals are frequently blocked by buildings, overpasses, and tunnels. Both experiments last about half an hour. The road vehicle is equipped with a Novatel OEM729 GNSS receiver and a Trimble AT1675-540TS GNSS antenna to acquire multi-frequency and multi-GNSS data. In addition, a tactical IMU is set in the vehicle to provide a reference trajectory by processing PPK and Inertial Navigation System (INS) with the data from the SBG IMU system.

Table 1 details the specific processing strategies used in the multi-frequency and multi-GNSS PPP-RTK system. The orbit and clock errors are corrected by the products provided by the Centre for Orbit Determination in Europe (CODE). The satellite phase biases are corrected by the UPD products estimated by an open-source software called GREAT-UPD (https://geodesy.noaa.gov/gps-toolbox/) using the aforementioned 29 GNSS stations. The UPDs and atmospheric corrections are updated every 5 s, while the sampling interval of observations at the user station is 1 s. The observations with elevation angle lower than 7° or the number of satellites in one epoch less than 4 are excluded.

Results

Evaluation of atmospheric corrections

To validate the atmospheric correction extraction method and the accuracy of the atmospheric corrections, stations A017, A018, and A019 from the Beijing regional network are selected as the reference stations,

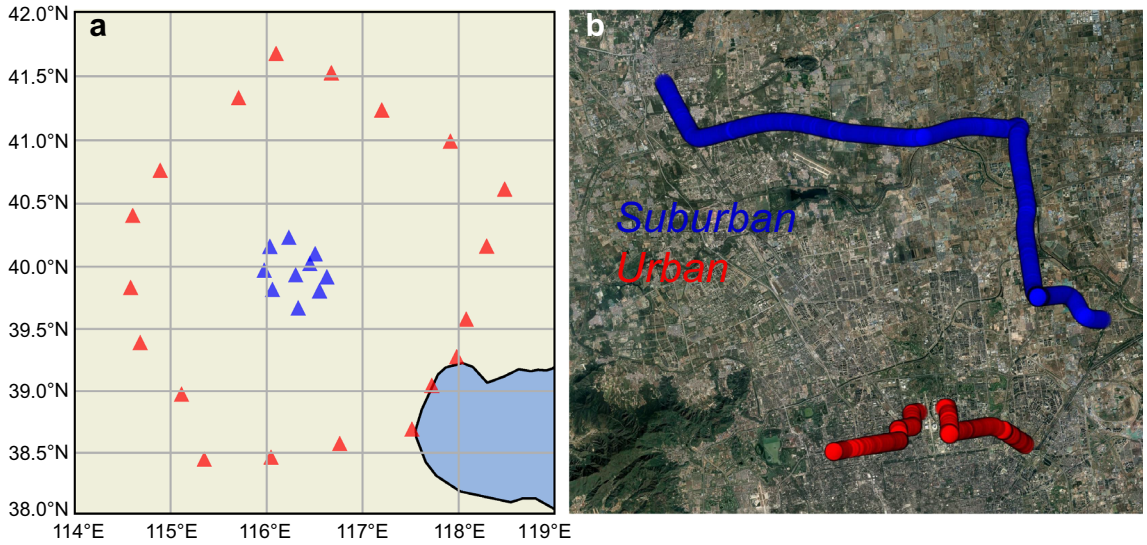

Fig. 3 **a** Distribution of 29 stations and **b** the trajectories of the experimental vehicle

Table 1 Processing strategy of multi-frequency and multi-GNSS PPP-RTK system

Items		Strategies	
GNSS system		GPS, Galileo and BDS	
GNSS signals		GPS: L1, L2 and L5; Galileo: E1, E5a, E5b, E5 and E6; BDS: B1I, B2I and B3I	
Combination mode		Raw observations	
Data sampling interval		Server: 5 s; User: 1 s	
Elevation mask		7°	
Minimum number of satellites		4	
Estimator		Sequential least squares	
Weight of observations		Elevation-dependent weight	
Phase wind-up effect		Corrected	
Satellite antenna phase center		Corrected by igs14.atx	
IFCB		Corrected by IFCB products	
Receiver antenna phase center		Corrected by igs14.atx	
Receiver clock		Epoch-wise estimated for each system and each frequency	
Phase ambiguities		EWL-WL-L1 cascade partial fixing	
Receiver coordinate		Server side	Fixed
		User side	Estimated in the epoch-wise kinematic model
Ionospheric delays		Server side	Epoch-wise estimated for each satellite
		User side	Corrected by precise ionospheric corrections
Tropospheric delays	Dry component	Modeled by Saastamoinen with Global Mapping function (GMF)	
	Wet component	Server side	Random-walk estimated
		User side	Corrected by precise tropospheric corrections

and used to interpolate the atmospheric corrections of station A022 which is regarded as the user station. The distribution of these four stations is shown in Fig. 4.

Based on the method proposed in Sect. 2.2, the original atmospheric corrections of these four stations are extracted. Then, the interpolated atmospheric corrections of the user station are obtained according to the MLCM mentioned in Sect. 2.3. The differences between the original and interpolated atmospheric corrections of station A022 are used to evaluate the accuracy of the atmospheric corrections. The difference results of zenith tropospheric corrections and slant ionospheric corrections for GPS, Galileo and BDS satellites are shown in Fig. 5, with solid dots in each color representing one satellite in Panel 1–3. It is visible that most of the differences are less than 1 cm. Some fluctuations are probably caused by the low elevation or short visible time of the satellite. The Root Mean Square (RMS) of slant ionospheric differences for GPS, Galileo, and BDS are 0.010, 0.008, and 0.006 m, respectively. Likewise,

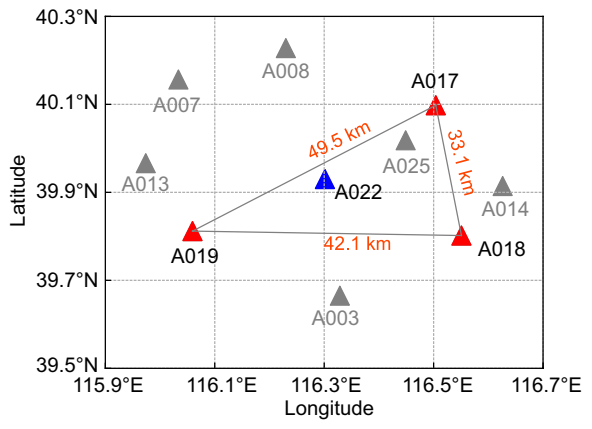

Fig. 4 Distribution of stations A017, A018, A019, and A022

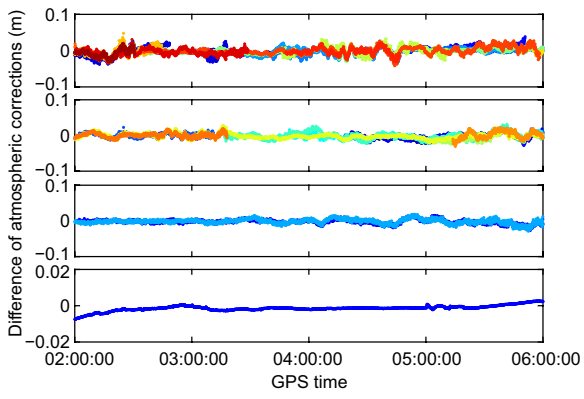

Fig. 5 Differences between the original and interpolated GPS, Galileo and BDS ionospheric corrections, and tropospheric corrections

Table 2 The statistical result of the DF GPS-only, the DF GEC and the MF GEC PPP-RTK

PPP-RTK Solution	RMS in different directions (m)			Fixing percentage (%)	TTFF (s)
	E direction	*N* direction	*U* direction		
DF GPS-only	0.134	0.159	0.280	68.60	1
DF GEC	0.035	0.048	0.099	87.80	1
MF GEC	0.019	0.017	0.035	93.70	1

Table 3 The statistical result of DF and MF GEC PPP-RTK

PPP-RTK solution	RMS in different directions (m)			Fixing percentage (%)	TTFF (s)
	E direction	*N* direction	*U* direction		
GF GEC	0.217	0.217	0.346	62.66	1
MF GEC	0.040	0.052	0.134	83.94	1

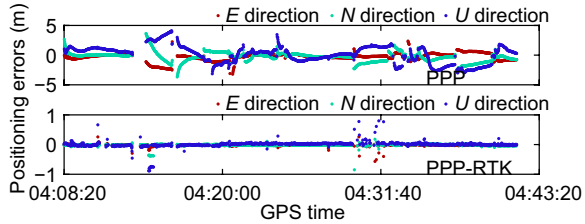

Fig. 6 DF GEC positioning series of PPP and PPP-RTK in the first experiment

the differences series of zenith tropospheric corrections is quite stable with the RMS value of 0.004 m. Our results indicate that the accuracy of the atmospheric corrections is at millimeter-level, which is sufficient for users to achieve PPP AR.

Performance of multi-frequency and multi-GNSS PPP-RTK

In order to comprehensively investigate the performance of the multi-frequency and multi-GNSS PPP-RTK, the results of PPP and PPP-RTK, single- and multi-GNSS PPP-RTK, Dual-Frequency (DF) and Multi-Frequency (MF) PPP-RTK, are compared, respectively. The performance of positioning solutions is evaluated in terms of positioning accuracy, fixing percentage, and TTFF. Here, the fixing percentage is calculated as the ratio of the number of epochs with fixed solution to total number of epochs. TTFF means the start time of a continuous 5 s fixed solution whose positioning errors are less than 5 cm in the horizontal direction and 10 cm in the vertical direction.

The first experiment was conducted in an open-sky suburban where the signals were interrupted by road signs, trees, and low-rise buildings occasionally. Figure 6 shows the DF GPS, Galileo, BDS (GEC) positioning series of PPP and PPP-RTK of the first experiment. The DF GEC PPP re-converges frequently due to the persistent signal interference, and the re-convergence commonly takes more than ten minutes. In some situations, the positioning accuracy of PPP even decreases to several meters. In contrast, the positioning series of DF GEC PPP-RTK is quite stable with a fast convergence in a few seconds. The RMS values of DF GEC PPP are 0.725, 1.005, and 1.467 m while those of DF GEC PPP-RTK are 0.035, 0.048, and 0.099 m in the east, north and vertical components, respectively. Compared to the DF GEC PPP solution, the PPP-RTK solution is capable of shortening the convergence time, and improving accuracy from meter-level to centimeter-level.

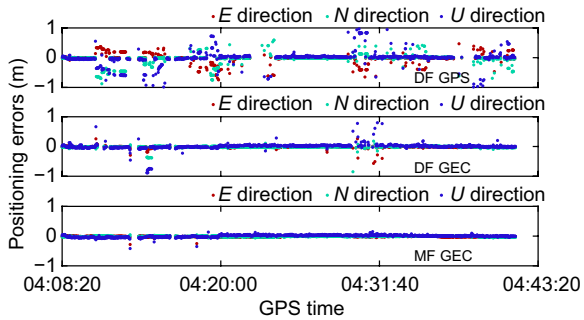

Fig. 7 Positioning series of DF GPS-only, DF GEC, and MF GEC PPP-RTK in the first experiment

Figure 7 shows the positioning series of the DF GPS-only, DF GEC, and MF GEC PPP-RTK in the first experiment. A number of outliers can be seen from the series of the DF GPS-only PPP-RTK, which indicates that the single-system PPP-RTK exhibits high instability in a kinematic environment. Compared to the DF GPS-only solution, the DF GEC PPP-RTK presents a more stable positioning series with fewer outliers, revealing a higher fixing percentage. Among all solutions, the MF GEC PPP-RTK exhibits the best performance with the highest positioning accuracy and the least outliers. The RMS values of the DF GPS-only PPP-RTK are 0.134, 0.159, and 0.280 m in the east, north and vertical components,

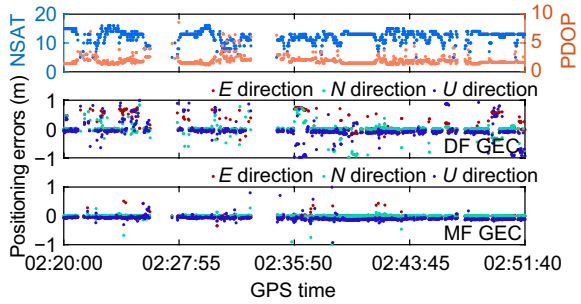

Fig. 8 NSAT and PDOP and positioning series of DF and MF GEC PPP-RTK in the second experiment

respectively (Table 2). With the multi-GNSS observations, the DF GEC PPP-RTK achieves the centimeter-level positioning accuracy of 0.035, 0.048, and 0.099 m in the east, north and vertical components, respectively. Compared to the DF GPS-only PPP-RTK, the corresponding improvement is 73.88%, 69.81%, and 64.64%, respectively. Better yet, because of the addition of multi-frequency signals, the MF GEC PPP-RTK shows the highest positioning accuracy of 0.019, 0.017, and 0.035 m in the east, north and vertical components. Compared to the DF GPS-only and the DF GEC PPP-RTK, the positioning accuracy has improved by 87.58% and 62.49%. Correspondingly, the fixing percentage is up to 93.70% which is increased by 25.10% and 5.90%, respectively. All three solutions can converge to centimeter-level accuracy in 1 s, but the GEC PPP-RTK shows the highest positioning accuracy and fixing percentage.

Figure 8 shows the number of the available GNSS satellites (NSAT) with precise atmospheric corrections and Position Dilution of Precision (PDOP) series and the positioning series of the DF and the MF GEC PPP-RTK in the second experiment. In the urban environment, the NSAT generally decreases to 12. The GNSS signals are seriously interrupted with high-rise buildings between 02:45:40 and 02:46:40 GPST, and completely blocked by a tunnel between 02:33:52 and 02:34:38. Compared to the DF GEC PPP-RTK, the MF GEC has a more precise and stable positioning series with fewer outliers, particularly when NAST series are sharply declining. In the environment with the signal greatly interrupted, the MF GEC PPP-RTK can still achieve AR with the constraint of EWL ambiguity, while GF cannot. The statistical results of positioning accuracy are given in Table 3. Compared to the GF GEC PPP-RTK, the positioning accuracy of the MF GEC PPP-RTK is improved from 0.217, 0.217, and 0.346 m to 0.040, 0.052, and 0.134 m, exhibiting the improvement of 81.57%, 76.04%, and 61.27% in the east, north, and vertical components. It can also be seen from Table 3 that the fixing percentage is improved from 62.66% to 83.94%. In general, the MF GEC PPP-RTK performs better and is able to meet the centimeter-level accuracy needed for urban positioning.

Table 4 The statistical result of DF and MF GEC PPP-RTK in Scenario (a)

PPP-RTK solution	RMS in different directions (m)			Fixing percentage (%)	TTFF (s)	Re-convergence time (s)
	E direction	*N* direction	*U* direction			
GF GEC	0.097	0.036	0.410	80.00	1	22
MF GEC	0.033	0.011	0.094	96.67	1	1

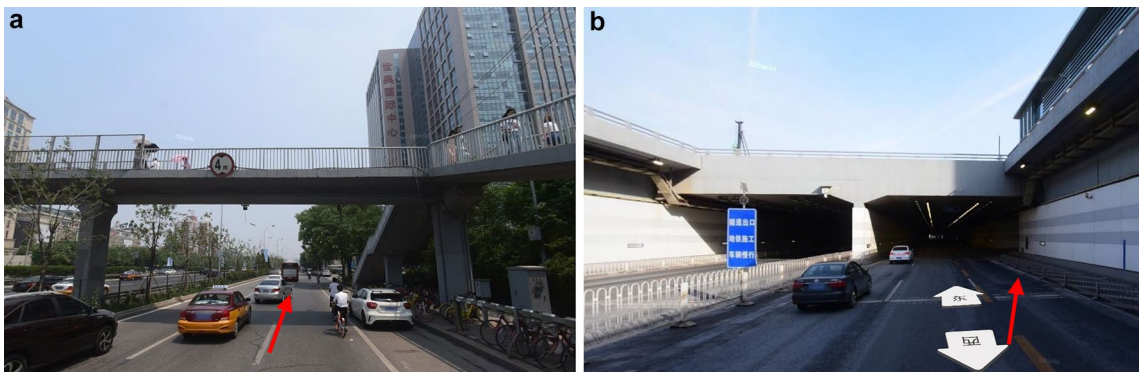

Fig. 9 **a** Observational environments in the overpass plus buildings scenarios and **b** tunnel plus buildings scenarios

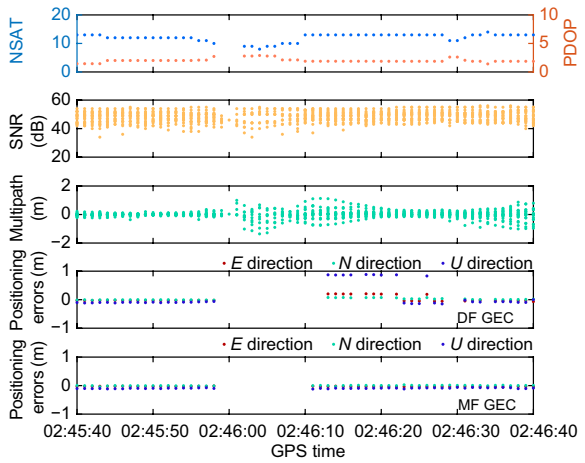

Fig. 10 NSAT, PDOP, SNR, multipath and positioning series of DF and MF GEC PPP-RTK in Scenario (**a**)

Multi-frequency PPP-RTK performance in different scenarios

Two scenarios, i.e., overpass plus buildings (Fig. 9a) and tunnel plus buildings (Fig. 9b) were selected to validate the benefits of MF signals for the GEC PPP-RTK. The observational environments for both scenarios are shown in Fig. 9. The experimental vehicle first passed through the overpass and then ran along the road with buildings on its sides in the first scenario, and in the second scenario it passed a tunnel with dense buildings in the entrance and exit of the tunnel.

In the first scenario, the experimental vehicle crossed the overpass at 02:45:58 GPST for four seconds. Then, the vehicle entered a road with dense buildings on its sides, where GNSS signals are seriously disturbed. The positioning series as well as the NSAT, PDOP, Signal–Noise-Ratio (SNR), and code multipath of the observation on the first frequency of GPS, Galileo and BDS series are shown in Fig. 10. The NSAT varies mostly between 12 and 14, and the corresponding PDOP is smaller than 2. It is also found that when the NSAT drops below 10, the PDOP value rises to above 2 between 02:45:58 and 02:46:09 GPST. Most of the SNRs range from 40 to 60 dB, but below 40 for the period 02:45:58 to 02:46:15 GPST. The code multipath series behave like a random noise series, where meter-level outliers exist from 02:46:00 to 02:46:20 GPST and 02:46:31 GPST to the end. In all likelihood, the loss lock of satellite and severe multipath contribute to the wrong fixing of ambiguity (Zhang & Li, 2013), leading to outlies in the positioning series of the DF solution between 02:46:13 and 02:46:26 GPST. Hence, as shown in Table 4, it takes 22 s to re-converge to a centimeter-level accuracy after crossing the overpass. Finally the RMS value in the vertical direction is 0.410 m and the fixing percentage is only 80.00%. Fortunately, with the constraint of the EWL ambiguity, the MF GEC PPP-RTK maintains high-precision and stable positioning throughout the experiment. Even though GNSS signals are interfered by buildings frequently, it realizes AR and centimeter-level positioning accuracy in 1 s. Therefore, a reliable fixed solution with a fixing percentage of 96.67%, and a higher positioning accuracy with the RMS values of 0.033, 0.011, and 0.094 m in the east, north and vertical components, respectively, is successfully achieved. Compared to the DF mode, the accuracy is improved by 76.31% and the fixing percentage is increased by 16.67%. We speculate that the addition of multi-frequency observations can resist the influence of multipath.

In the second scenario, the vehicle went downhill starting at 02:32:20 GPST where the NSATs gradually decreased to 10 as shown in Fig. 11. During the period from 02:32:52 to 02:34:30 GPST, the vehicle was crossing the tunnel where the signals were completely lost. Afterward, the vehicle left the underground tunnel and the

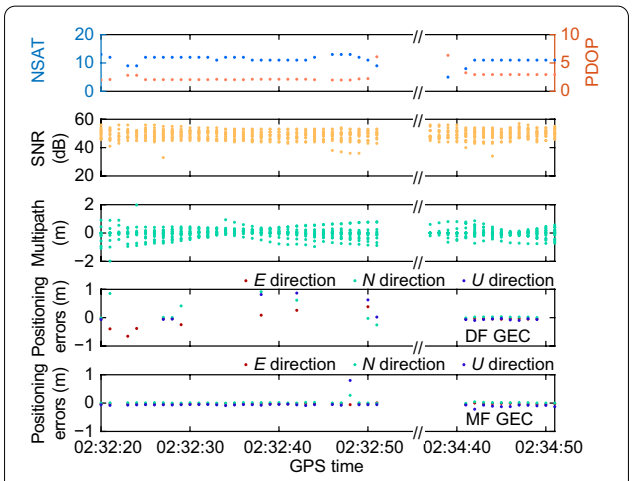

Fig. 11 NSAT, PDOP, SNR, multipath and positioning series of DF and MF GEC PPP-RTK in Scenario (**b**)

Table 5 The statistical result of the DF and MF GEC PPP-RTK in Scenario (b)

PPP-RTK solution	RMS in different directions (m)			Fixing percentage (%)	TTFF (s)	Re-convergence time (s)
	E direction	*N* direction	*U* direction			
GF GEC	0.338	0.533	0.769	40.38	–	3
MF GEC	0.029	0.045	0.148	80.77	1	1

signal intensity gradually increased. The majority of SNR series is between 40 and 60 dB, and the values of multipath effect are most in the range of ± 1.5 m. The positioning series of the DF GEC PPP-RTK cannot converge to centimeter-level accuracy until the vehicle leaving the tunnel. In contrast, the MF GEC PPP-RTK maintains a more precise, stable and complete positioning results when GNSS signals are available. It is worth noting that there are still some places where the positioning results are missing or have large errors due to the obscuration of the buildings. The statistical results of the two solutions are given in Table 5. Compared to the DF GEC PPP-RTK, the MF improves accuracy from the RMS of 0.338, 0.533, and 0.769 m to RMS of 0.029, 0.045, and 0.148 m in the east, north and vertical components, respectively. Although the both solutions cannot achieve a high fixing percentage under such a complex environment, the MF GEC PPP-RTK still greatly improved the fixing percentage from 40.38% to 80.77%. After the vehicle left the tunnel, an instantaneous ambiguity resolution can be achieved with the MF GEC PPP-RTK while it requires more time with dual-frequency mode.

Conclusions

In this contribution, we developed a multi-frequency and multi-GNSS PPP-RTK method aiming to achieve rapid positioning with the centimeter level accuracy for vehicle navigation in urban environments. In the proposed method, with multi-frequency and multi-GNSS observations the precise atmospheric corrections are derived from the server side and disseminated to the user side to achieve the aim.

Beijing regional network was selected to extract the precise atmospheric corrections. The internal accuracy of atmospheric corrections is better than 1 cm. Vehicle experiments were conducted in suburban and urban environments to verify the performance of the multi-frequency and multi-GNSS PPP-RTK. In the suburbs, the MF GEC PPP-RTK performs best. Compared to the DF GPS-only PPP-RTK solution, the positioning accuracy is improved from the RMS of 0.134, 0.159, and 0.280 m to that of 0.019, 0.017, 0.035 m in the east, north and vertical components with an improvement of 87.58%, and the fixing percentage is increased from 68.60% to 93.70%. In an urban environment where GNSS signals are interfered frequently, the MF GEC PPP-RTK still provides the most precise, reliable and continuous positioning results, because of the enhancement of the multi-frequency signals. Compared to the DF GEC PPP-RTK solution, the positioning accuracy is improved from the RMS of 0.217, 0.217, and 0.346 m to the RMS of 0.040, 0.052, and 0.134 m in the east, north and vertical components, with the fixing percentage improved from 62.66% to 83.94%.

Moreover, the performance of the proposed method in the overpass and the tunnel scenarios was assessed. The results show that accuracy of within 5 cm in the horizontal direction and within 15 cm in the vertical direction, and the TTFF of 1–3 s can be achieved. The fixing percentage is 96.67% in the overpass scenario, while 80.77% in the tunnel scenario. Even though GNSS signals are interfered by the buildings or blocked by the tunnel, AR and centimeter-level positioning accuracy can be achieved in 3 s.

The results of the above experiment indicate that the multi-frequency signals can resist the influence of multipath on the PPP-RTK, and significantly improve the accuracy and reliability of the PPP-RTK in the urban environment where GNSS signals are interrupted frequently. The MF GEC PPP-RTK always performs better than the GF GEC PPP-RTK, and much better than the DF GPS-only PPP-RTK and the DF GEC PPP. Therefore the proposed multi-frequency and multi-GNSS PPP-RTK method can greatly improve the availability of vehicle navigation in urban environments.

Acknowledgements
The numerical calculations in this paper have been done on the supercomputing system in the Supercomputing Center of Wuhan University.

Authors' contributions
XL and BW proposed the idea, processed the GNSS data of vehicle navigation, and wrote this paper. XL and HL assisted in paper writing and revision. JH and XH contribute to the data acquisition and discussion on data analysis. All authors read and approved the final manuscript.

Funding
This work has been supported by the National Natural Science Foundation of China (Grant 41974027 and Grant 41974029), the Sino-German mobility program (Grant No. M0054), and the Technology Innovation Special Project (Major program) of Hubei Province of China (Grant No. 2019AAA043).

Availability of data and materials
The datasets used and analyzed in this study are available from the corresponding author on reasonable request.

Declarations

Competing interests
The authors declare that they have no competing interests.

Author details
[1]School of Geodesy and Geomatics, Wuhan University, 129 Luoyu Road, Wuhan 430079, China. [2]Technische Universitat Berlin (TUB), Straße des 17. Juni, 10623 Berlin, Germany.

Received: 8 December 2021 Accepted: 2 March 2022
Published online: 11 April 2022

References

Cabinet Office. 2020. Quasi-Zenith Satellite System performance standard (PS-QZSS-002). https://qzss.go.jp/en/technical/download/pdf/ps-is-qzss/ps-qzss-002.pdf?t=1618040032826.
European GNSS Agency (2019). PPP-RTK market and technology report.

Geng, J., & Bock, Y. (2013). Triple-frequency GPS precise point positioning with rapid ambiguity resolution. *Journal of Geodesy, 87*(5), 449–460.
Geng, J., Guo, J., Meng, X., et al. (2020). Speeding up PPP ambiguity resolution using triple-frequency GPS/BeiDou/Galileo/QZSS data. *Journal of Geodesy, 94*, 6. https://doi.org/10.1007/s00190-019-01330-1
Gu, S., Lou, Y., Shi, C., & Liu, J. (2015). BeiDou phase bias estimation and its application in precise point positioning with triple-frequency observable. *Journal of Geodesy, 89*(10), 979–992.
Guo, F., Zhang, X., & Wang, J. (2015). Timing group delay and differential code bias corrections for BeiDou positioning. *Journal of Geodesy, 89*(5), 427–445.
Jokinen, A., Feng, S., Schuster, W., Ochieng, W., Hide, C., Moore, T., & Hill, C. (2013). GLONASS aided GPS ambiguity fixed precise point positioning. *Journal of Navigation, 66*(3), 399–416.
Kouba, J., & Heroux, P. (2001). Precise point positioning using IGS orbit and clock products. *GPS Solut, 5*(2), 12–28.
Kouba J. 2015. A guide to using international GNSS service (IGS) products. http://kb.igs.org/hc/en-us/articles/201271873-A-Guide-to-Using-the-IGS-Products.
Khodabandeh, A., & Teunissen, P. J. G. (2016). PPP-RTK and inter-system biases: The ISB look-up table as a means to support multi-system PPP-RTK. *Journal of Geodesy, 90*(9), 837–851. https://doi.org/10.1007/s00190-016-0914-9
Li, X., Zhang, X., & Ge, M. (2011). Regional reference network augmented precise point positioning for instantaneous ambiguity resolution. *Journal of Geodesy, 85*(3), 151–158. https://doi.org/10.1007/s00190-010-0424-0
Li, X., Ge, M., Zhang, H., & Wickert, J. (2013). A method for improving uncalibrated phase delay estimation and ambiguity-fixing in real-time precise point positioning. *Journal of Geodesy, 87*, 405–416. https://doi.org/10.1007/s00190-013-0611-x
Li, X., Ge, M., Douša, J., & Wickert, J. (2014). Real-time precise point positioning regional augmentation for large GPS reference networks. *GPS Solutions, 18*(1), 61–71.
Li, X., Li, X., Yuan, Y., Zhang, K., Zhang, X., & Wickert, J. (2018). Multi-GNSS phase delay estimation and PPP ambiguity resolution: GPS, BDS, GLONASS, Galileo. *Journal of Geodesy, 92*, 579–608. https://doi.org/10.1007/s00190-017-1081-3
Li, X., Li, X., Liu, G., et al. (2019). Triple-frequency PPP ambiguity resolution with multi-constellation GNSS: BDS and Galileo. *Journal of Geodesy, 93*, 1105–1122. https://doi.org/10.1007/s00190-019-01229-x
Li, X., Han, X., Li, X., et al. (2021). GREAT-UPD: An open-source software for uncalibrated phase delay estimation based on multi-GNSS and multi-frequency observations. *GPS Solut, 25*, 66. https://doi.org/10.1007/s10291-020-01070-2
Liu, Y., Song, W., Lou, Y., Ye, S., & Zhang, R. (2017). GLONASS phase bias estimation and its PPP ambiguity resolution using homogeneous receivers. *GPS Solutions, 21*(2), 427–437.
Montenbruck, O., Hauschild, A., Steigenberger, P., & Langley, R. B. (2010). Three's the challenge: A close look at GPS SVN62 triple-frequency signal combinations finds carrier-phase variations on the new L5. *GPS World, 21*(8), 8–19.
Montenbruck O, Hauschild A, Steigenberger P. (2014). Differential code bias estimation using multi-GNSS observations and global ionosphere maps. Navigation: Journal of The Institute of Navigation 61(3), 191–201.
de Oliveira, P. S., Morel, L., Fund, F., Legros, R., Monico, J. F. G., Durand, S., & Durand, F. (2017). Modeling tropospheric wet delays with dense and sparse network configurations for PPP-RTK. *GPS Solutions, 21*(1), 237–250.
Pan, L., Zhang, X., Li, X., Liu, J., & Li, X. (2017). Characteristics of inter-frequency clock bias for Block IIF satellites and its effect on triple-frequency GPS precise point positioning. *GPS Solutions, 21*(2), 811–822. https://doi.org/10.1007/s10291-016-0571-8
Pan, L., Li, X., Zhang, X., Li, X., Lu, C., Zhao, Q., & Liu, J. (2017). Considering inter-frequency clock bias for BDS triple-frequency precise point positioning. *Remote Sensing, 9*(7), 734. https://doi.org/10.3390/rs9070734
Pan, L., Zhang, X., Guo, F., & Liu, J. (2019). GPS inter-frequency clock bias estimation for both uncombined and ionospheric-free combined triple-frequency precise point positioning. *Journal of Geodesy, 93*(4), 473–487.
Ren, X., Zhang, J., Chen, J., Zhang, X.(*) (2021). Ionospheric Modeling by using Multi-GNSS and upcoming LEO Constellations: Two Methods and Comparison. In IEEE Transactions on Geoscience and Remote Sensing, 1–15
Teunissen, P., Odijk, D., & Zhang, B. (2010). PPP-RTK: Results of CORS network-based PPP with integer ambiguity resolution. *J Aeronaut Astronaut Aviat Ser A, 42*(4), 223–230.
Wubbena G, Schmitz M, Bagg A (2005) PPP-RTK: Precise point positioning using state-space representation in RTK networks. In: Proceedings of ION GNSS, pp 13–16.
Zhang, B., Teunissen, P. J. G., & Odijk, D. (2011). A novel un-differenced PPP-RTK concept. *Journal of Navigation, 64*(S1), S180–S191.
Zhang, B., Chen, Y., & Yuan, Y. (2019). PPP-RTK based on undifferenced and uncombined observations: Theoretical and practical aspects. *Journal of Geodesy, 93*(7), 1011–1024.
Zhang, B., Ou, J., Yuan, Y., et al. (2012). Extraction of line-of-sight ionospheric observables from GPS data using precise point positioning. *Science China Earth Sciences, 55*, 1919–1928. https://doi.org/10.1007/s11430-012-4454-8
Zhang, X., & Li, P. (2013). Assessment of correct fixing rate for precise point positioning ambiguity resolution on a global scale. *Journal of Geodesy, 87*, 579–589.
Zumberge, J. F., Heflin, M. B., Jefferson, D. C., Watkins, M. M., & Webb, F. H. (1997). Precise point positioning for the efficient and robust analysis of GPS data from large networks. *Journal of Geophysical Research, 102*(B3), 5005–5017. https://doi.org/10.1029/96JB03860

Publisher's Note